

# Time-varying EEG spectral power predicts evoked and spontaneous fMRI motor brain activity

Neil Mehta,<sup>1,2\*</sup> Inês Gonçalves,<sup>1\*</sup> Alberto Montagna<sup>1</sup>, Mathis Fleury<sup>1</sup>,  
Gustavo Caetano<sup>1</sup>, Inês Esteves<sup>1</sup>, Athanasios Vourvopoulos<sup>1</sup>,  
Pulkit Grover,<sup>2</sup> Patrícia Figueiredo<sup>1</sup>

<sup>1</sup>Institute for Systems and Robotics – Lisboa and Department of Bioengineering,  
Instituto Superior Técnico, Universidade de Lisboa, Portugal

<sup>2</sup>Electrical and Computer Engineering Department,  
Carnegie Mellon University

\* Authors contributed equally.

April 16, 2025

**Keywords:** simultaneous EEG-fMRI, time series prediction, cross-modal prediction, EEG-fMRI temporal null models

**Abstract:** Simultaneous EEG-fMRI recordings are increasingly used to investigate brain activity by leveraging the complementary high spatial and high temporal resolution of fMRI and EEG signals respectively. It remains unclear, however, to what degree these two imaging modalities capture shared information about neural activity. Here, we investigate whether it is possible to predict both task-evoked and spontaneous fMRI signals of motor brain networks from EEG time-varying spectral power using interpretable models trained for individual subjects with Sparse Group Lasso regularization. Critically, we test the trained models on data acquired from each subject on a different day and obtain statistical validation by comparison with appropriate null models as well as the conventional EEG sensorimotor rhythm. We find significant prediction results in most subjects, although less frequently for resting-state compared to task-based conditions. Furthermore, we interpret the model learned parameters to

understand representations of EEG-fMRI coupling in terms of predictive EEG channels, frequencies, and haemodynamic delays. In conclusion, our work provides evidence of the ability to predict fMRI motor brain activity from EEG recordings alone across different days, in both task-evoked and spontaneous conditions, with statistical significance in individual subjects. These results present great potential for translation to EEG neurofeedback applications.

## 1 Introduction

Simultaneous electroencephalogram and functional magnetic resonance imaging (EEG-fMRI) is a valuable multimodal tool in human neuroscience, due to the complementary information about brain function provided by the two imaging modalities (Jorge et al., 2014; Warbrick, 2022). EEG is a direct measure of neuronal activity, providing high temporal resolution information of changing local field potentials; however, due to volume conduction of electric currents through the brain, skull, and scalp, EEG suffers from limited spatial specificity, as well as coverage. In contrast, fMRI provides exquisite spatial resolution with full brain coverage; however, it is an indirect measure of neuronal activity based on blood-oxygenation-level-dependent (BOLD) fluctuations reflecting neurovascular coupling mechanisms. The integration of EEG and fMRI from simultaneous recordings was initially motivated by the need to improve the localization of epileptic brain networks generating the abnormal electrical discharges observed in EEG. It was then extended to study healthy brain function, with the first studies aiming to map BOLD-fMRI activity associated with well-known EEG phenomena such as the alpha rhythm. Although such EEG-informed fMRI approaches have been the most common, a variety of both asymmetric and symmetric integration techniques have been employed to analyze simultaneous EEG-fMRI data (Abreu et al., 2018).

Recently, a growing interest has developed in the inverse problem of identifying EEG features associated with brain activity patterns measured using BOLD-fMRI. A fundamental motivation is to provide evidence of the neuronal correlates of various phenomena observed using BOLD-fMRI, ultimately contributing to the realization of the potential for the integration of multimodal EEG-fMRI data (Murta et al., 2015). A practical motivation to address this problem of cross-modal reconstruction is the design of neurofeedback (NF) protocols based on EEG only (Fleury et al., 2023). In particular, NF during the execution of motor imagery tasks has been explored for the neurorehabilitation of stroke patients, by promoting brain plasticity and recovery of lost or impaired motor function (Vourvopoulos et al., 2019). Typically, NF signals are based on the EEG sensorimotor rhythm (SMR), which has long been known to be a marker of activity originating in the sensorimotor brain areas, and is characterized by a reduction in alpha ( $\sim$ 8-12 Hz) and beta ( $\sim$ 13-30 Hz) power, known as event-related desynchronization (ERD) (Pfurtscheller &

Lopes da Silva, 1999; Pfurtscheller et al., 2006). Unfortunately, motor imagery NF systems have not been successful in many patients, probably due to the well-known difficulty in measuring the EEG SMR. In fact, it is estimated that NF signals such as the SMR, which are used to control brain computer interfaces (BCIs), cannot be measured in about 15-30% of the general population, a phenomenon known as BCI illiteracy. Alternatively, fMRI allows the representation of specific brain regions and networks, and could provide more robust NF signals. However, it carries considerably higher costs, as well as safety, portability, and accessibility limitations. Hence, it would be of great interest to develop EEG-only NF protocols that could (also) target brain activity patterns measured using fMRI.

With this motivation, in a seminal study Meir-Hasson et al., 2014 used penalized linear regression based on EEG spectral power from a single electrode to obtain an EEG Finger-Print (EFP) of the BOLD-fMRI activity of the amygdala during a neurofeedback task. The authors further demonstrated that the EFP was significantly more predictive than a traditional EEG theta/alpha activity. In a series of follow-up works, the authors expanded their approach from a subject-specific to a group model (Meir-Hasson et al., 2016), and further showed that it was effective in helping subjects downregulate their amygdala activity compared to a sham group, ultimately improving implicit emotion regulation (Keynan et al., 2016). Inspired by the EFP approach, others developed similar predictive models for different brain regions in a diverse set of neuromodulation applications (Or-Borichev et al., 2023; Rudnev et al., 2021; Singer et al., 2023). In Cury et al., 2020, the authors moved beyond the single electrode EFP approach and developed a sparse regression model utilizing multi-channel EEG time-frequency features to predict EEG-fMRI NF scores from EEG signals during motor imagery. Simões et al., 2020 employed a different approach, using random forests instead of linear regression, as well as a wide selection of EEG-derived features beyond spectral power, to predict the BOLD-fMRI activity of the facial expression processing network. The few works involving resting-state activity addressed different questions, demonstrating the ability to relate whole-brain EEG and fMRI connectomes, or the ability of EEG microstates to predict fMRI functional connectivity states (Abreu et al., 2021; Deligianni et al., 2014; Zoubi et al., 2022). A growing body of literature has used deep learning in different problems of EEG-fMRI prediction (Afrasiyabi et al., 2025; Calhas & Henriques, 2020, 2022a, 2022b, 2023; Kovalev et al., 2022; Li, Lou, Xu, Wang, & Chang, 2024; Li, Lou, Xu, Zhang, et al., 2024; Liu et al., 2020, 2022; Roos et al., 2025; Yao et al., 2025).

Despite the relative success of previous attempts, the ability of EEG models to predict concurrent somatomotor BOLD activity remains to be fully demonstrated. It is not clear, for example, to what extent spontaneous BOLD fluctuations may be predicted in comparison to task-evoked activity. In the present work, we develop models to predict the BOLD-fMRI activity of the somatomotor network (SMN) from concurrent EEG signals, during the execution of motor imagery tasks as well as in resting state. We choose interpretable distributed lag linear models with explanatory variables comprising time-frequency

representations of present and recent past EEG signals. Models are trained using EEG-fMRI data acquired from a subject on one day and tested using data acquired from the same subject on a different day. Models are compared to a literature-informed predictor based on the conventional wisdom surrounding SMR.

The key contributions of this work include:

- The emphasis on contrasting predictive power of EEG signals for BOLD-fMRI in both spontaneous and task-evoked conditions.
- The assessment of statistical significance of learned models for EEG-to-fMRI prediction using appropriate and specific temporal null models.
- The accurate quantification of test-retest reliability of prediction models, a key determining factor in their use for neurofeedback protocols.
- Full model transparency and interpretation of learning coefficients in terms of relevant spatial, frequency, and temporal features for capturing EEG-fMRI coactivation patterns.

## 2 Methods

In this section, we first describe the dataset, including the participants, experimental protocol, and data acquisition details, as well as the EEG and fMRI data analysis pipelines used to extract the signal time series subsequently used for EEG-fMRI modeling. The final subsection describes the modeling approach, including model definition, estimation, selection, and validation.

### 2.1 Participants and Experimental Protocol

Fifteen healthy volunteers (7 females, 8 males; mean age:  $24.4 \pm 2.7$  years) participated in this study. The study was approved by Hospital da Luz Ethics Committee, and all participants provided written informed consent. For each subject, simultaneous EEG-fMRI data were acquired in two separate sessions approximately 2 weeks apart.

In each session, subjects were studied during the performance of two motor imagery tasks (Graz and NeuRow) and during a resting-state period (Rest). One task involved motor imagery only based on the Graz paradigm (Graz), while the other task also included observation of a first-person perspective of

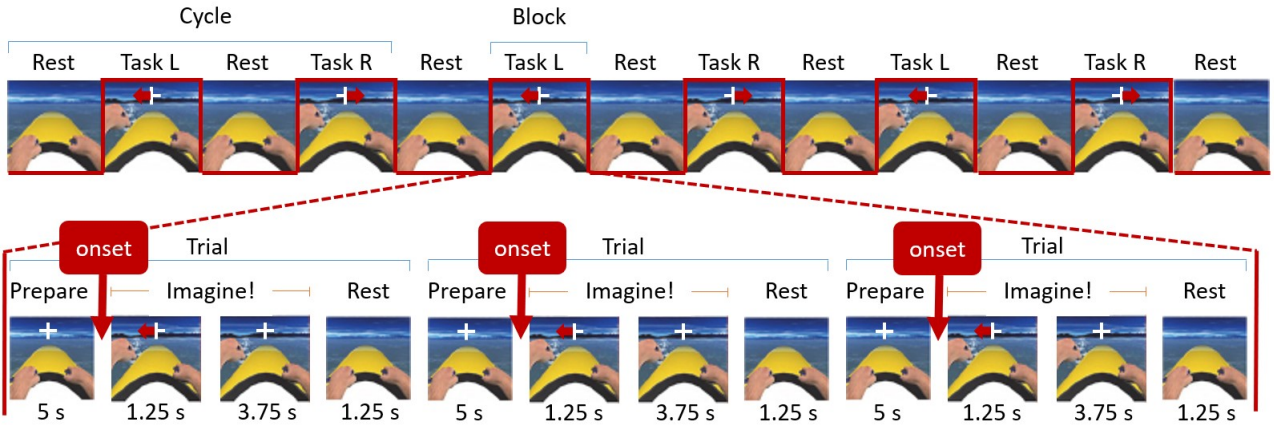


Figure 1: *Experimental protocol for one run of motor imagery task: structure of the run (top) and one block of trials (bottom).* Blocks of left and right arm tasks (Task L and Task R) are separated by blocks of rest (Rest). Each trial is initiated with a preparation period and ends with a brief rest before the next trial. The illustration pertains to the NeuRow task, during which both the arrow and the rowing arm avatar are presented. For the Graz task, the protocol timings are identical but only the arrow is presented to the subject.

two virtual avatar arms on a boat with two paddles (NeuRow) (Nunes et al., 2023; Vourvopoulos et al., 2016). In both tasks, participants were instructed to imagine the kinesthetic experience of rowing using either their left or right arm, over blocks of three consecutive trials each, interleaved with rest. In Graz, a simple directional arrow served as the cue (left or right) against a black background with a white fixation cross. In NeuRow, the same arrow and fixation cross were presented, but this time superimposed on the virtual avatar arm displaying the instructed movement. Stimulus presentation was implemented using Unity, a game engine software, and was presented in synchronization with the EEG and fMRI acquisitions using NeuXus (Caetano et al., 2023; Legeay et al., 2022). The tasks were performed over 3 runs. The time structure of a run is illustrated in Fig. 1. Each run comprised 3 cycles, alternating 1 block of left arm imagery and 1 block of right arm imagery with rest blocks. Each block included 3 trials alternated with rest. Each trial was indicated by a fixation cross, and consisted of 5s preparation followed by 1.25s of arrow cue and 3.75s of imagery. During rest periods, a simple black screen (Graz) or a static avatar (NeuRow) were presented. In each session, subjects performed a total of 54 trials (27 for each arm) over  $\sim$ 17 mins per task. During Rest acquisitions, participants were instructed to lie still for 10 min while keeping their eyes open in dim light.

## 2.2 EEG-fMRI Data Acquisition

MRI scans were acquired using a 3T Siemens Vida system with a 64-channel-receive head radio-frequency coil. Functional images were acquired using a 2D Echo-Planar Imaging (EPI) sequence (TR = 1260 ms; TE = 30 ms; flip angle = 70°; voxel size = 2.2 mm isotropic; in-plane acceleration with GRAPPA factor 2; simultaneous multi-slice with SMS factor 3; 60 axial slices). Structural images were acquired using a T1-weighted magnetization-prepared rapid gradient echo (MPRAGE) sequence (TR = 2300 ms; TE = 2.98 ms; voxel size = 1.0 mm isotropic). EEG data were collected using a 32-channel MR-compatible EEG system (Brain Products GmbH, Germany), including 31 EEG channels and 1 electrocardiogram (ECG) channel. The EEG electrodes were placed on the head according to the 10-20 system, and the ECG electrode was placed on the back. The data were acquired using BrainVision Recorder (Brain Products, Germany) at a sampling rate of 5 kHz.

## 2.3 EEG-fMRI Data Analysis

### 2.3.1 fMRI Data Preprocessing

Functional images were preprocessed using FMRIB Software Library (FSL) (Smith et al., 2004). A standard pipeline was followed, as described in the literature (Jenkinson et al., 2002), including: distortion correction using a fieldmap image, motion correction and realignment to the middle volume using rigid body transformation, removal of non-brain structures, high-pass temporal filtering (0.01 Hz cutoff frequency), spatial smoothing (3.3 mm full width at half maximum (FWHM) Gaussian kernel), co-registration to the structural image, and normalization to the Montreal Neurological Institute 152 (MNI152) standard space.

For resting-state data, an additional denoising step was performed, in which the following nuisance time series were regressed out of the data: the six estimated motion parameters (MPs), motion outliers (MOs) identified as volumes for which the RMS intensity difference relative to adjacent volumes was above the 75th percentile plus 1.5 times the interquartile range, and the average white matter (WM) and cerebrospinal fluid (CSF) signals obtained from masks defined by segmentation of the structural image.

### 2.3.2 Extraction of fMRI Signals

For each motor imagery task (Graz and NeuRow), subject, session and run, the preprocessed fMRI data were submitted to a first-level voxelwise general linear model (GLM) analysis using FSL's tool FEAT. The GLM was defined by convolving the square waveform of the task paradigm, for left and right-arm trials, with the canonical haemodynamic response function (HRF), as given by a double-gamma function with an overshoot at 6 seconds relative to onset. Additionally, its temporal derivative, the six MPs and the MOs were included as confounding regressors. Whole-brain images representing task-evoked activations were derived by fitting the GLM to each voxel's BOLD time series. To identify the group brain activation patterns associated with each task, a group-level mixed-effects GLM analysis was performed on the parameter estimates of the regressor of interest, and one-sample t-tests were converted to z-statistics and thresholded with a voxelwise threshold of  $z > 3.1$ , and an FWE-corrected cluster-level threshold of  $p < 0.05$ .

The thresholded z-statistic images previously obtained for each subject, session, and run were binarized and then multiplied by a binary mask of the group-level activation map. This was performed to ensure that each region of interest (ROI) was task-relevant, by removing voxels from non-motor areas or that showed no significant activation on average. A BOLD time series representative of the trial-evoked activity (TE) was obtained by averaging the BOLD signals across voxels within each ROI for each task, subject, session, and run. A BOLD time series representative of the trial-by-trial fluctuations (TBT) was obtained by averaging the residuals of the voxelwise GLM across voxels within each ROI for each task, subject, session, and run. Both the TE and TBT time series were converted to percent signal change with respect to the baseline, which was defined as the temporal mean of the BOLD signal in the period before the first trial in each run. After standardization of each run, the 3 runs were concatenated for each session.

The preprocessed fMRI data were subjected to group Independent Component Analysis (ICA) using FSL's tool MELODIC. The number of independent components (ICs) was set to 30, as a compromise between under-fitting and over-fitting (Wang & Li, 2015). The z-statistic maps of the resulting ICs were thresholded at  $z > 3.1$  and the SMN was identified as the IC yielding the maximum Dice coefficient between its map and Yeo's template of the corresponding canonical RSN (Yeo et al., 2011). Dual regression was then performed to obtain the SMN map and corresponding BOLD time series in each subject and session. This was converted to percent signal change with respect to the baseline, which was defined as the temporal mean of the BOLD signal over the whole run.

### 2.3.3 EEG Data Preprocessing

EEG data were preprocessed in MATLAB (MathWorks, 2023) using code developed in-house ([LaSEEBGithub](#)) based on tools from the open-source toolbox EEGLAB (Abreu et al., 2016, 2018; Delorme & Makeig, 2004). First, the gradient artifact (GA) was removed using moving average template subtraction. Additionally, an optimal basis set (OBS) extracted with principal component analysis (PCA) was used to fit and remove the residuals, implemented in the EEGLAB-plugin FMRIB (Smith et al., 2004). The ECG R-peaks were detected using a Long Short-Term Memory (LSTM) network, and manually corrected when needed, and the EEG data were then corrected for the pulse artifact (PA) using a combination of ICA and the optimal basis set (OBS) technique (Abreu et al., 2016). Following MR artifact correction, EEG data were downsampled to 250 Hz and bandpass filtered from 1 to 40 Hz. Hereafter, bad EEG channels were removed, all EEG channels were re-referenced to their average, and subjected to ICA to identify and remove physiological artifacts such as muscle activity and eye movement artifacts from the data. Finally, interpolation of burst activity was performed using Artifact Subspace Reconstruction (ASR) (Chang et al., 2020).

### 2.3.4 Extraction of EEG Features

Feature extraction was performed using Brainstorm (Tadel et al., 2011). The time-varying power spectra were extracted from each of the 31 EEG channels (excluding ECG) by application of the continuous wavelet transform using a complex Morlet mother wavelet with a central frequency of 1 Hz and a time resolution of 3 s (Bertrand & Tallon-Baudry, 2000; Pantazis et al., 2005). We extracted wavelet coefficients for each whole number frequency in the range 1-40 Hz and approximated the time-varying relative power by squaring the coefficients and dividing by the total power across the spectrum at each sample in time.

For the TBT conditions, an additional step was performed of removing the average trial-evoked response for both left and right trials. Practically, this process involved epoching the EEG time-frequency data in each channel over 10 seconds windows centered on each trial onset and averaging across trials in each run to produce a stereotype of the subject's response to the task. This stereotype was then subtracted from the relative power time series at each trial to leave only trial-by-trial fluctuations.

We temporally downsampled these power time series using an anti-aliasing low-pass filter to match the sampling rate of the BOLD signal. In the case of the tasks Graz and NeuRow, we standardized EEG relative power regressors for each run and then concatenated them across the 3 runs of each session.

## 2.4 EEG-fMRI Modeling

To summarize, for each subject and session, BOLD-fMRI signals were extracted in the five following conditions: 1) Graz - TE; 2) NeuRow - TE; 3) Graz - TBT; 4) NeuRow - TBT; and 5) Rest. While conditions 1) and 2) correspond to brain activity evoked by task trials, conditions 3) to 5) correspond to spontaneous fluctuations in brain activity, either from trial to trial during the execution of a task (3 and 4) or during rest (5). In the following sections, we describe the modeling decisions and estimation techniques employed to generate informed time series predictions of the BOLD signal for each subject, session and condition.

### 2.4.1 Massive Univariate Correlation Analysis

As a preliminary analysis, and to compare the coefficients of the learned models against, for each condition, subject and session, we computed the Pearson correlation between each EEG regressor (frequency-specific power time series from each EEG channel) and the concurrent BOLD time series, by shifting the EEG signals forward relative to the BOLD signal by the following haemodynamic lags,  $\{0, 1, 2, \dots, 8\}$  TRs.

### 2.4.2 Model Definition

To accommodate the known temporal lag of the BOLD signal relative to the EEG signal, we constructed a *distributed lag model* (DLM) i.e. a linear model that includes individual regressors for each EEG channel and frequency, as well as lagged copies of each of these time series. The input data is a tensor,  $X \in \mathbb{R}^{T \times C \times F}$ , where  $T$ ,  $C$ , and  $F$  represent the duration of the EEG signal ( $T = 804$ ), the number of channels ( $C = 31$ ), and the number of frequencies ( $F = 40$ ), respectively. Let  $y \in \mathbb{R}^T$  denote the true BOLD signal derived as in 2.3. Flattening our input tensor,  $X$ , to form a design matrix,  $\mathcal{X} \in \mathbb{R}^{T \times R}$  where  $R = C \times F$ , allows us to express this model as follows,

$$y = \beta \mathcal{X} + \epsilon = \beta_0 + \sum_{r \in [R]} (\beta_r^{(0)} L^0 \mathcal{X}_r + \beta_r^{(1)} L^1 \mathcal{X}_r + \dots + \beta_r^{(M-1)} L^{M-1} \mathcal{X}_r) + \epsilon \quad (1)$$

where the sum is taken over the total number of regressors across all channels and frequencies,  $R$ , and  $L^n x_t = x_{t-n}$  is the lag operator of order  $n$ . Individual coefficients  $\beta_r^{(n)}$  account for the effects of each of these regressors, at the specific lag  $n$  up to a maximum specified lag order,  $M - 1$ . The errors,  $\epsilon$ , are assumed to be normally distributed and uncorrelated in time. Based on the range of previously reported haemodynamic lags, as well as our preliminary massive univariate correlation analysis presented in Fig. 5,

we include the EEG time sample aligned with the current fMRI sample we are attempting to predict as well as the previous 8 time points (fMRI acquisitions), corresponding to approximately 10s ( $M = 9$ ).

### 2.4.3 Model Estimation

The model we have specified is high-dimensional and surely multicollinear due to our inclusion of high-resolution frequency information and lagged copies of each regressor. Further, the number of samples in our dataset is much less than the number of regressors. Both of these properties are known to cause identifiability and stability issues during model estimation. To deal with these issues, we considered different methods of *structured sparsity regularization*.

We opted for the Sparse Group Lasso (Simon et al., 2013) formulation due to the natural hierarchical structure of our EEG features based on grouping regressors according to EEG channel and frequency. The Sparse Group Lasso problem is formulated as follows,

$$\beta^* = \arg \min_{\beta} \frac{1}{2n} \|y - \sum_{c \in C} \beta_{(c)} \mathcal{X}_{(c)}\|_2^2 + \lambda(1 - \alpha) \sum_{c \in C} \sqrt{p_c} \|\beta_{(c)}\|_2 + \lambda\alpha \|\beta\|_1 \quad (2)$$

The tradeoff between  $\ell_1$  and  $\ell_2$  regularization penalties are controlled by  $\alpha$ , while  $\lambda$  controls the overall strength of regularization. Scaling the group penalty by the length of  $\beta_{(c)}$ ,  $\sqrt{p_c}$ , ensures that distinct group sizes do not influence the optimization. The Sparse Group Lasso is a tradeoff between unconstrained and group-constrained sparsities. In our use case, the EEG channels form a natural grouping for constrained sparsity since smoothness in learned coefficients for each EEG channel across lags and frequencies is desirable. If we choose the maximum lag,  $M - 1$ , to be large enough, then the combination of these regularization terms will ensure that regressors (including lagged regressors) that do not provide unique information will have zero coefficients, which will help model interpretability. The specified model parameters are estimated using a variant of the Fast Iterative-Shrinking Threshold Algorithm (FISTA) for its efficiency (Moe, 2019).

### 2.4.4 Model Selection

We perform block  $k$ -fold cross validation ( $k = 3$ ) to optimize the regularization hyperparameters,  $\alpha$  and  $\lambda$ . The choice of a block cross-validation scheme preserves the ordering of samples in time, which is important not to contaminate the training and validation partitions by allowing serially correlated samples to appear in training and validation partitions simultaneously. The cross-validation scheme is illustrated

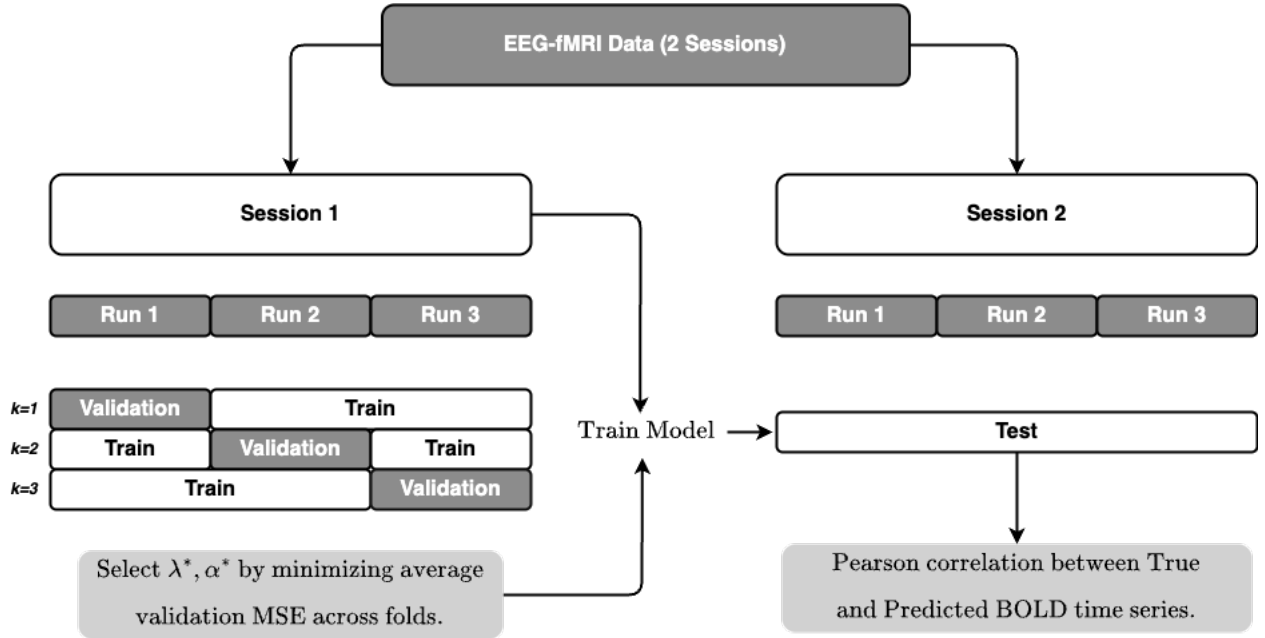


Figure 2: *Nested Cross-Validation Scheme*. In the first iteration, the first session is used for training and validation partitions to select values for hyperparameters. A model is then trained with these values and the entirety of the session data. The trained model is evaluated on the held-out session of data. Finally, the two sessions are exchanged and the process repeated.

in Fig 2.

For the task data (Graz and NeuRow), we exploit our protocol structure (a session contains 3 runs) and compose our training and validation partitions as including or excluding whole runs of the experiment. To be specific, each run of a session is a validation partition once during the optimization and the other two runs in the same session are used for training data. The remaining session is held out as the test set. For Resting State, although we no longer have separate runs, we adhere to the block  $k$ -fold scheme by dividing the recorded data in to 3 equal size contiguous blocks.

To speed up hyperparameter tuning, we utilize Bayesian optimization (Nogueira, 2014) to preferentially sample the mean squared error (MSE) of our model predictions versus the true BOLD time series on our validation partitions. This choice allows us to quickly reach a sufficient approximation of the validation loss surface minimum as compared to a grid search approach. To select candidate hyperparameter values based on previously estimated hyperparameter pairs, we use a standard choice of utility function, the Upper Confidence Bound, with  $\kappa = 0.1$ . Because our model is convex, we can be certain that we reach an approximation of a global minimizer in a finite number of steps using a low value for  $\kappa$ , which prioritizes exploitation as opposed to exploration.

The final choice of hyperparameter values is made by averaging all sampled MSE values across validation

partitions. A Gaussian process regression is then fitted to develop an estimation of the validation loss surface from all observed samples during the Bayesian optimization step. The minimizer of this estimated loss surface defines our optimal  $\alpha$  and  $\lambda$  values. A model is then trained on all of the training data (one entire session) using these values and applied to the test set to generate a predicted BOLD time series.

The Pearson correlation between the predicted time series and the true BOLD time series is computed and used as the discriminating statistic to assess the generalization performance of our learned model. Once a model is estimated for a specific subject and condition using one session's worth of data as the training set, we swap sessions and repeat. The averaged performance over both sessions is our final estimate of generalization performance for all analyses unless otherwise stated.

#### 2.4.5 Model Validation

To ascertain the statistical significance of the model's predictions, we utilize the *method of surrogates* (Lancaster et al., 2018). This method involves generating a large number of surrogate samples of BOLD time series consistent with an appropriate null hypothesis and applying the model estimation procedure to these surrogate time series to obtain a null distribution associated with our null hypothesis. The p-value of the chosen discriminating statistic is then computed under the null distribution.

Our null hypothesis is that the BOLD time series cannot be explained by any linear combination of EEG features at any lag. *Fourier Transform surrogates (FT)* are commonly used to generate surrogate sample time series that preserve the autocorrelation function and power spectral density of the original time series. A model trained with unperturbed EEG time series and FT surrogates of the BOLD time series is consistent with the null hypothesis. However, this surrogate generation procedure may admit false positives if our initial BOLD time series is produced via a non-Gaussian stochastic process, or if it is non-stationary. To mitigate non-Gaussianity, we utilize the variant *Iterative Amplitude-Adjusted Fourier Transform (IAAFT)* surrogates (Lancaster et al., 2018), which avoids false positives due to non-Gaussianity by adjusting the amplitude distribution of the final surrogate to better match the initial starting time series. To mitigate non-stationarity, we preemptively test each BOLD time series using the Augmented Dicky-Fuller test (ADF) to ensure stationarity ( $p < 10^{-5}$  for all time series).

For each BOLD surrogate time series, a model is estimated based on the unperturbed EEG time series, and its generalization performance is measured using Pearson correlation between predicted and true surrogate time series (as for the true BOLD time series). This correlation represents a realization of the distribution of the null hypothesis. To assess the statistical significance of the model's prediction for each subject, session, and condition, a null distribution is obtained by generating 100 surrogates. P-values

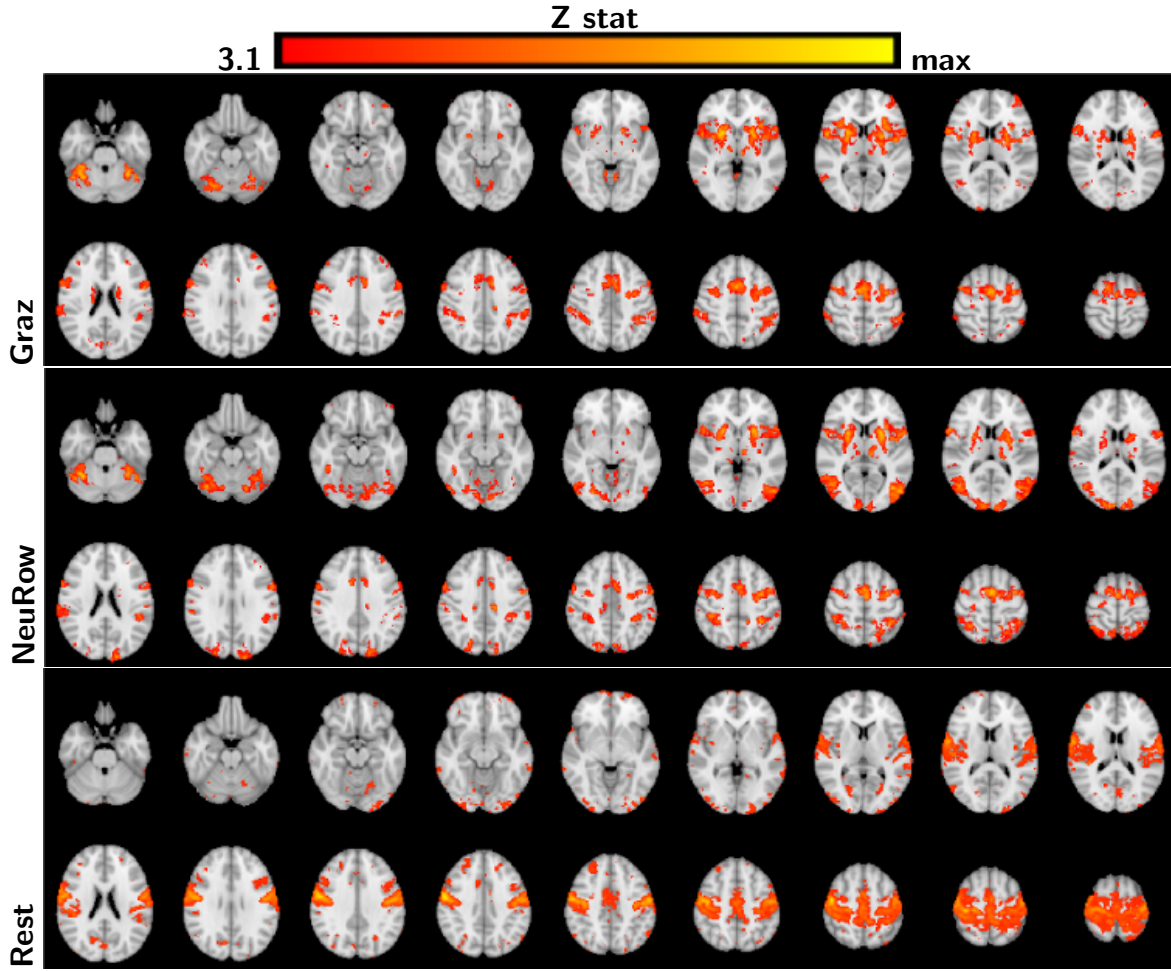


Figure 3: *BOLD-fMRI SMN maps*. Group SMN maps identified for both tasks as the average motor imagery activation across subjects and sessions (Graz, Neurow), and for rest by group ICA and subsequent identification of the SMN network by template matching (Rest). The Z statistic maps obtained after thresholding for statistical significance (color) are overlaid on the MNI anatomical brain template (gray).

are computed as the number of surrogate models for which the Pearson correlation is greater than or equal to the Pearson correlation between predicted and true BOLD signals, normalized by the number of surrogates.

#### 2.4.6 Comparison with Conventional SMR Model

To further assess the value of the predictions obtained with the learned models, we compared with the ones obtained using a conventional SMR model, which was not learned from the data but rather based on previous literature. We defined our conventional SMR model by averaging activities from C3 and C4 channels in the alpha and beta bands (8-30 Hz), and shifting it relative to the BOLD signal by 6.3 s (corresponding to a canonical hemodynamic delay).

### 3 Results

In this section, we first present the results of the fMRI analysis leading to the mapping of the SMN and extraction of the respective BOLD activity time courses. We then present the results of the preliminary massive univariate EEG-fMRI correlation analysis, before presenting the results of the model estimation in detail, including the subject-level model validation against a null model as well as the group-level comparison of the learned models with the conventional SMR model.

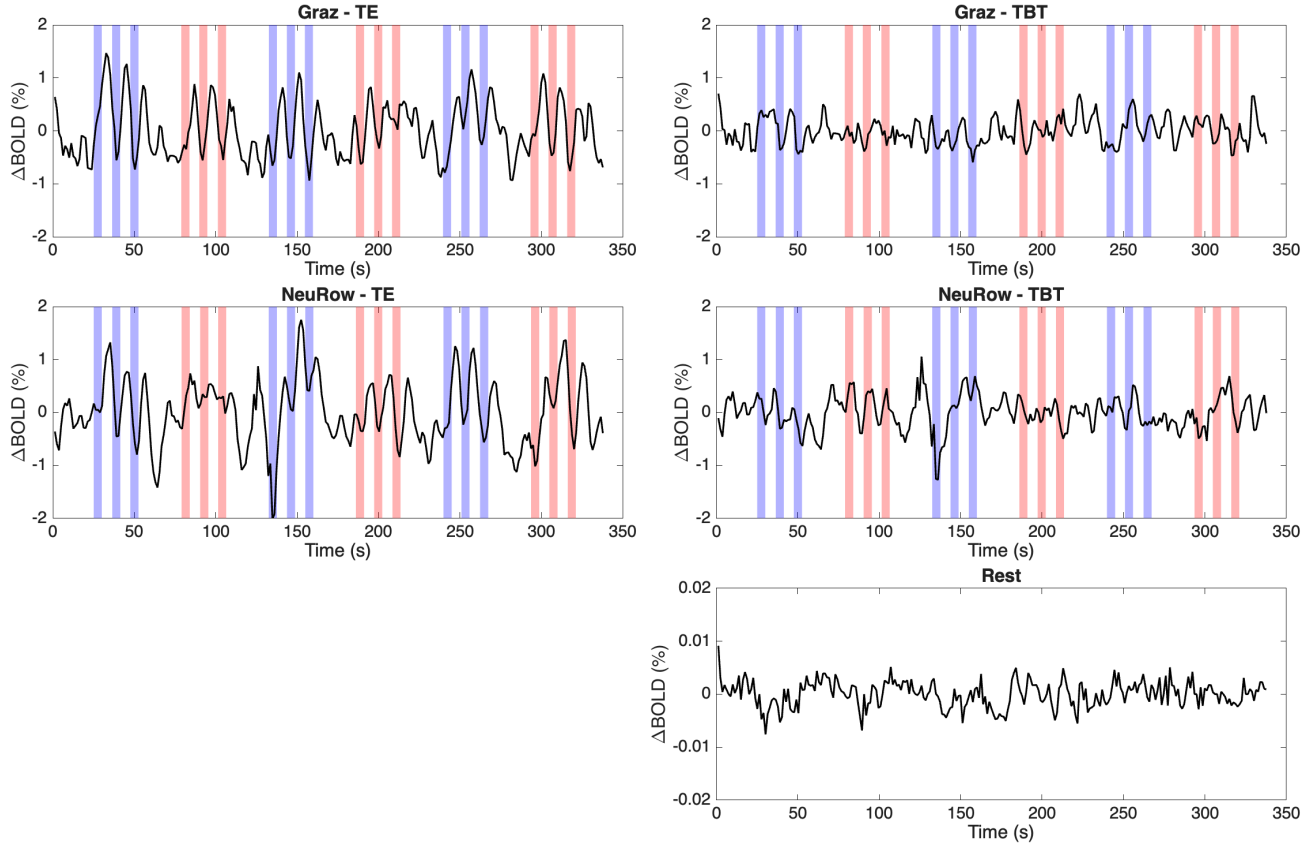


Figure 4: *BOLD-fMRI SMN timeseries*. Illustrative example of the BOLD-fMRI time series obtained from the SMN map in each condition (Graz - TE, Graz - TBT, NeuRow - TE, NeuRow - TBT, and Rest), for a representative period of approximately 350 seconds from a session of one subject. The vertical red and blue lines indicate trials of left and right arm motor imagery. A clear modulation of the BOLD-fMRI signal can be appreciated in the two trial-evoked time courses (left), which is not observed in the trial-by-trial fluctuations or rest (right), as expected.

#### 3.1 fMRI SMN mapping and BOLD time series extraction

The group-level maps of the SMN obtained for the motor imagery tasks (Graz and NeuRow) and the resting state (Rest) are shown in Fig. 3. An illustrative example of the fMRI time series obtained for

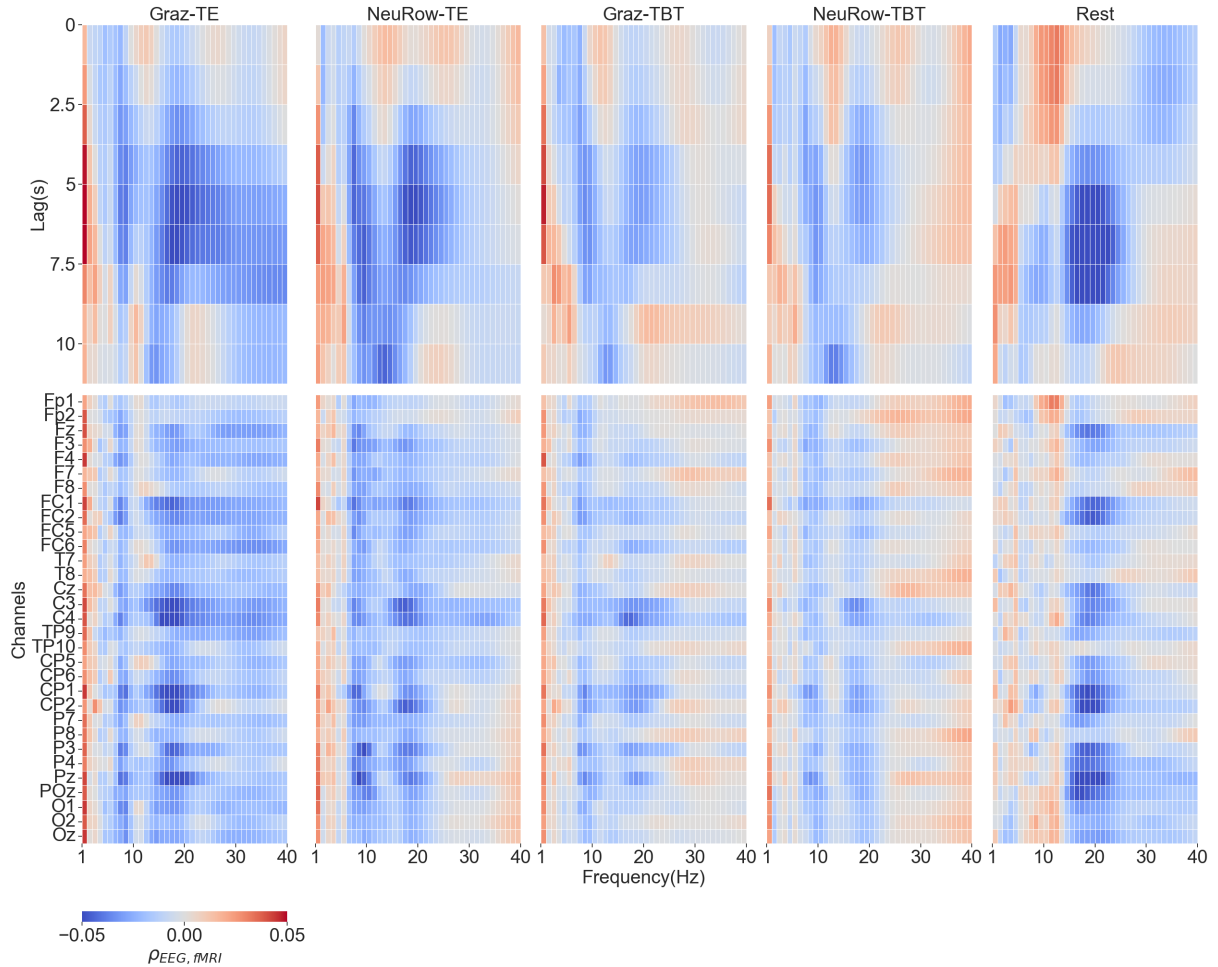


Figure 5: *EEG-fMRI Massive Univariate Correlation Analysis*. Pearson correlation values averaged across subjects and sessions, for each of the five conditions tested (Graz - TE, NeuRow - TE, Graz - TBT, NeuRow - TBT, Rest): (Top) Heatmaps of correlation values averaged across lags, as a function of frequency and channel, arranged from anterior to posterior brain regions from top to bottom. (Bottom) Heatmaps of correlation values averaged across channels, as a function of frequency and lag.

the five conditions (Graz - TE, Graz - TBT, NeuRow - TE, NeuRow - TBT, and Rest) in an individual subject are shown in Fig. 4.

### 3.2 EEG-fMRI Massive Univariate Correlation Analysis

The mass univariate temporal correlations between the SMN BOLD-fMRI activity and concurrent EEG power features are presented in Fig. 5, averaged across subjects and sessions, for each of the five conditions tested. For simplicity of visualization, 2D heatmaps are shown, by averaging the correlation coefficients across lags (frequencies  $\times$  channels) or across channels (frequencies  $\times$  lags).

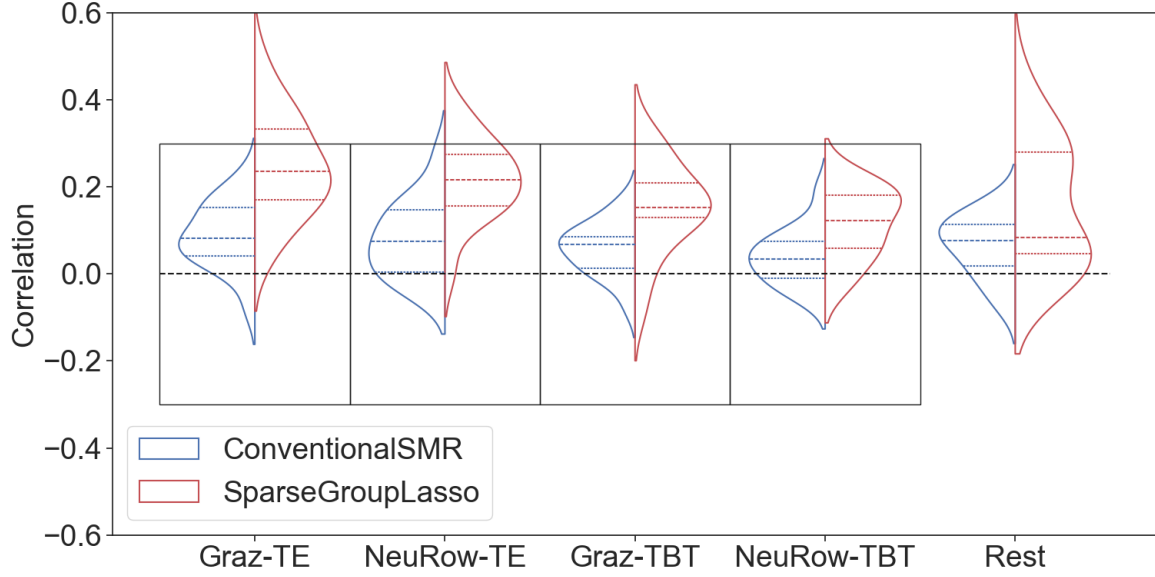


Figure 6: *EEG-to-fMRI Prediction: Comparison of estimated model with conventional SMR model.* Test performance of estimated models and conventional SMR models in each condition. Each violin plot represents the kernel density estimate of the distribution of test performance (average of correlations across sessions) across the 15 subjects. Dashed and dotted lines indicate median and IQR limits, respectively. Solid boxes indicate statistically significant differences between estimated and conventional SMR models (From left to right,  $p = \{0.0018, 0.0002, 0.0057, 0.0004, 0.0855\}$ , Mann-Whitney U test with Bonferroni correction for multiple comparisons,  $\alpha = 0.05$ ).

### 3.3 EEG-to-fMRI Prediction: Comparison with Conventional SMR Model

The group-level evaluation of the test performance of the estimated models compared to the respective conventional SMR models is presented in Fig. 6. Using a Mann-Whitney U test, we found that the estimated models achieved significantly better test correlations than the respective conventional SMR models for both conditions of the motor imagery tasks, but not for Rest. These results suggest we benefit from other sensor locations and frequency components beyond C3 and C4 alpha/beta activity predictors. Further analysis of which channels and frequencies are important predictors of simultaneous BOLD activity with respect to different conditions is presented in 3.5.

### 3.4 EEG-to-fMRI Prediction: Model Validation

The test performance of the models estimated to predict SMN BOLD-fMRI activity from concurrent EEG power features, in each subject and session, for each of the five conditions tested, is presented in Fig. 7. In each case, we compare the model discriminating statistic (Pearson correlation between predicted and true BOLD time series) to the respective null distribution, and indicate cases where a

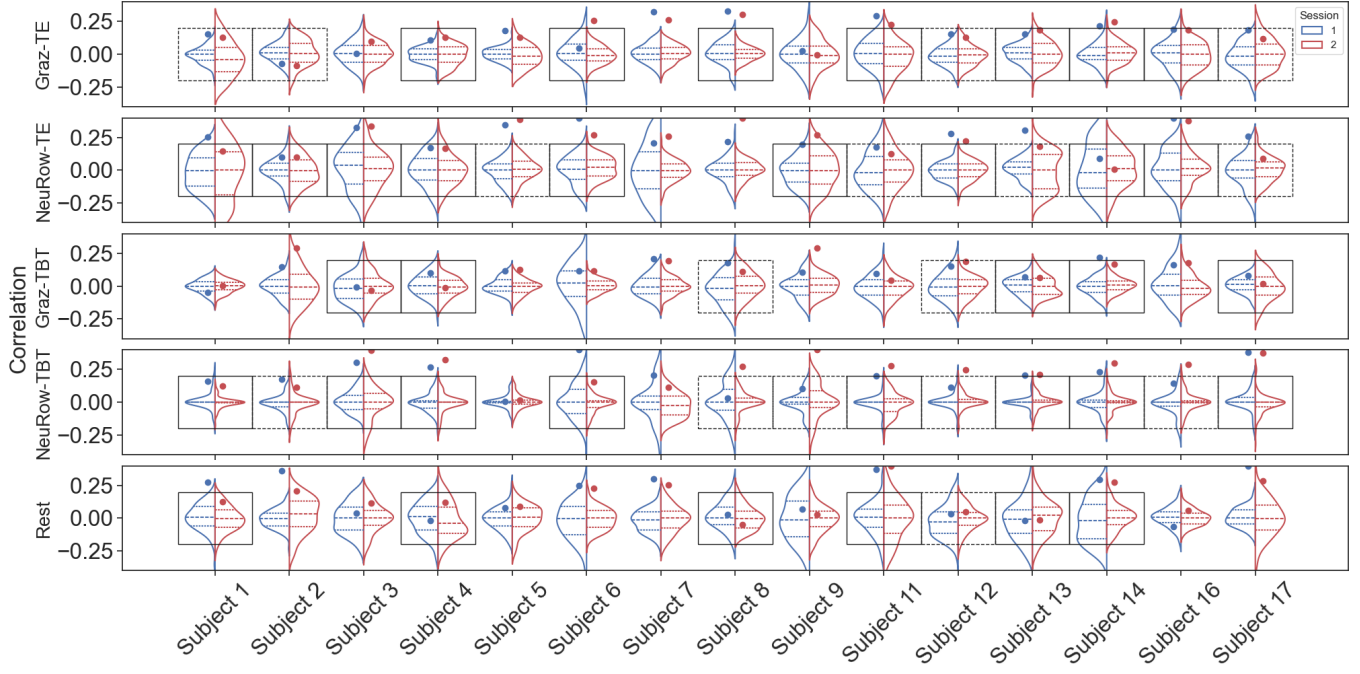


Figure 7: *Test Performance of EEG-to-fMRI Models: Validation against Null Distributions.* Each row represents one of the five conditions, while columns correspond to individual subjects, including both prediction from session 1 to session 2 and vice-versa (blue and red). Dots represent the test correlation of the estimated model in each case, while the violin plots represent the kernel density estimate of the subject/session-specific null distributions. The boxes denote whether a subject's models were significant (solid for both, dashed if only a single model was significant).

statistical significance difference was found.

Table 1 summarizes the number of models for which a significant prediction was achieved, for either one or both sessions, within each condition. While a significant prediction was achieved for at least one session in most subjects in the TE conditions for both Graz and NeuRow tasks, this number was reduced in TBT of NeuRow and in Rest. Of particular note, subjects 5 and 7 produced almost no significant predictions in any condition.

Table 1: Summary of Significant Models

Condition	Task	One	Both	Total
<b>Task-evoked</b>	Graz - TE	4	9	22 / 30
	NeuRow - TE	5	8	21 / 30
<b>Spontaneous</b>	Graz - TBT	4	7	18 / 30
	NeuRow - TBT	2	5	12 / 30
	Rest	1	6	13 / 30

### 3.5 EEG-to-fMRI Prediction: Model Interpretability

To assess whether the estimated models are physiologically meaningful, we exploited the interpretability of the linear models used and analyzed the patterns of model coefficients. The model coefficients, average across subjects and session, are presented in Fig. 8, arranged such that the EEG frequencies, channels, and hemodynamic lags that are important for predicting concurrent BOLD signals are clear. Recall from 2.4.2 that a coefficient is estimated for each regressor in a  $C \times F \times M$  tensor. To simplify the visualization of the results, we follow the same approach as for the massive univariate correlation analysis and show 2D heatmaps, by averaging the coefficients across lags (frequencies  $\times$  channels) or across channels (frequencies  $\times$  lags).

## 4 Discussion

We demonstrate that it is possible to predict both evoked and spontaneous BOLD activity of motor brain networks based on interpretable EEG models trained on EEG-fMRI data acquired from the same subject on a different day. The learned models are not only significantly better than conventional EEG SMN features in most conditions, but to varying degrees they exhibit a significant predictive power in most subjects when compared with null models. Importantly, trial-by-trial fluctuations during a motor imagery task and resting-state activity can also be predicted even if with lower fidelity than task-evoked activity.

### 4.1 Relation to literature

Ours is the first study aiming to predict the BOLD activity of the motor network from concurrent EEG. Nevertheless, one other study addressed a very similar problem, that of predicting EEG-fMRI NF scores from EEG signals, employing a similar penalized linear regression approach (Cury et al., 2020). In contrast to this study, we employed a Sparse Group Lasso regularization, allowing us to achieve informative spatial sparsity while maintaining smoothness in the temporal and frequency domains. Moreover, we created appropriate null models to assess the statistical significance of the predictions in each subject. Most importantly, we went beyond task-evoked activity to investigate the ability of the models to predict even spontaneous fMRI signals, either across trials or during rest.

More generally, most previous works aiming to predict fMRI signals from EEG also leveraged the well-known relationship between EEG oscillatory activity and BOLD-fMRI activation (Formaggio et al., 2010; Murta et al., 2015; Scheeringa et al., 2012). However, most reduced either the spatial dimension (for

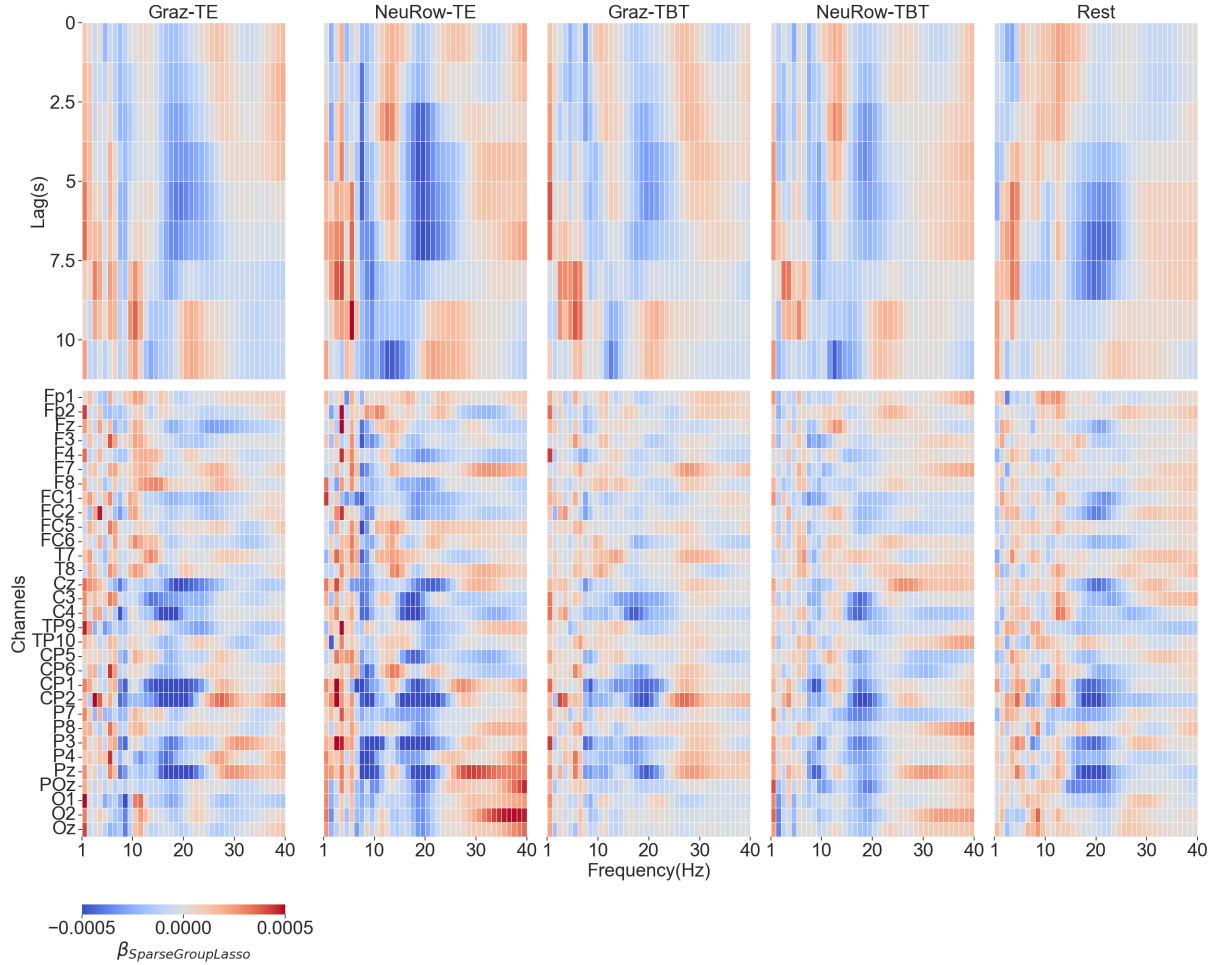


Figure 8: *EEG-to-fMRI Model Interpretability*. Model coefficients averaged across subjects and sessions, for each of the five conditions tested: (Top) Heatmaps of correlation values averaged across lags, as a function of frequency and channel, with anterior to posterior brain regions arranged from top to bottom. (Bottom) Heatmaps of correlation values averaged across channels, as a function of frequency and lag.

example, the use of a single EEG electrode in EFP models as described in Meir-Hasson et al., 2014, 2016) and/or using only EEG SMR frequencies (alpha and beta) (Cury et al., 2020). Instead, we opted to preserve the full spatial and frequency resolution of EEG signals to allow our model to estimate relevant relationships in a data-driven fashion. Importantly, the model we employed strikes a balance between complexity and expressivity as compared to modern deep learning approaches to also allow for rigorous model validation and significance testing.

## 4.2 Prediction significance

The results of our surrogate data analysis demonstrate that the statistical significance of fMRI signal predictions from concurrent EEG signals using models trained in a separate session depends strongly on whether we aim to predict task-evoked or spontaneous activities. In fact, it was possible to achieve significant predictions of task-evoked activity (Graz - TE and NeuRow - TE) for over 70% of the subjects and sessions. However, this was reduced to about 50% for spontaneous activities, either trial-by-trial during the tasks (Graz - TBT and NeuRow - TBT) or during rest (Rest).

This is expected; however, it is clear that there is still some residual correlation between EEG and BOLD-fMRI in the trial-by-trial fluctuations. This is demonstrated by comparing the Graz - TBT and NeuRow - TBT conditions to the Rest condition. Since, the Rest condition data is derived from separate sessions in which no task stimulus was provided, it represents a setting in which there is no task-evoked coupling between the two modalities. The relatively stronger significance of the trial-by-trial fluctuation conditions as compared to the resting-state condition implies that there is still some coupling between the two modalities in the absence of task-relevant activities *during* the execution of a task. It is a testament to the power of our models that even without task-evoked activity, significant correlations are still detectable between EEG and BOLD-fMRI time series.

## 4.3 Model interpretability

The EEG-fMRI massive univariate correlation patterns were generally consistent with the expected SMR (shown in Fig. 5). We found negative correlations of fMRI motor brain activity with EEG power in the alpha and/or beta bands (8 - 30 Hz), consistently with the desynchronization in these frequencies (Pfurtscheller & Lopes da Silva, 1999). Interestingly, two sub-bands were clearly evident in our case, one in the lower alpha band, ~8-9 Hz, and another one in the beta band, ~15-20 Hz. Also as expected, although this correlation pattern was spread throughout the brain, it was nevertheless strongest in channels C3-C4, near the somatomotor cortex, and also in the parietal channels CP1-CP2 and P3-P4-Pz, as has been previously observed in motor imagery tasks (Batista et al., 2024). Moreover, the hemodynamic lags that produced the strongest correlations were centered around the canonical value of about 6 seconds (Logothetis et al., 2001) but varied considerably across frequencies. Altogether, although such univariate computation does not account for interactions between EEG regressors, it nevertheless informed us that, despite a predominance of negative correlations in the alpha/beta ranges around central electrode locations, and for canonical haemodynamic delays, a more complex distribution across frequencies, channels and delays clearly sets the motivation for the features included in our models.

In fact, by analysing the learned model coefficients (Fig. 5), we found a large degree of agreement with the massive univariate correlation patterns. Interestingly, the learned coefficients show distinctively sparser patterns, suggesting that the Sparse Group Lasso penalty was effective in learning a smooth but sparsified approximation of the massive univariate correlations, with redundant and uninformative predictors removed. This effect was especially pronounced spatially, with the channels nearest the somatomotor cortex (Cz-C3-C4) and parietal regions (CP1-CP2 and Pz-P3-P4) exhibiting the strongest negative correlations across all conditions in both  $\sim$ 8-10 Hz and  $\sim$ 15-25 Hz frequency ranges, which suggests our grouping of covariates by EEG channel was effective in promoting spatial sparsity.

## 4.4 Limitations and future work

Important limitations of this work arise from certain modelling assumptions. Broadly, the choice of a linear model improves interpretability and reliability of statistical inferences made about the implicated physiological time series. The assumptions of normally distributed and independent errors are violated if the underlying generative process of the BOLD time series is non-Gaussian, but generally linear regression is robust for most scenarios which violate this assumption. The independence of errors is directly violated by the observed autocorrelations of the BOLD time series. Though non-stationarity null hypotheses were rejected for all fMRI time series, recent works suggest that frequently-used fMRI preprocessing packages may suboptimally prewhiten fMRI time series (Olszowy et al., 2019), which could admit more false positives during surrogate data testing. These issues in addition to the high dimensionality and data scarcity present estimation difficulties, which may cast doubt on the achieved evaluation metrics presented. To preempt these concerns, we have carefully designed our surrogate data test to remove undesirable inclusion criteria from our null hypothesis. These preemptive measures include using the Augmented Dicky-Fuller test to remove potential false positives due to non-stationarity of the BOLD time series and also the choice of IAAFT surrogates to circumvent false positives arising from non-Gaussianity of the underlying generative process of BOLD time series.

The issue of BCI illiteracy may also impact our conclusions. Two specific subjects in our analysis performed poorly across most if not all task conditions. In order to understand if subjects 5 and 7 may be BCI illiterate, we intend to investigate whether their ERD is reduced compared to other subjects, as well as, whether they had higher prevalence of motion outliers in their recordings.

Future work will address the potential variability in EEG-fMRI coupling over time as our recent analyses have demonstrated rapid switching between distinct correlation states (data not shown). We intend to exploit these findings to inform our model prediction.

Because our model is high-dimensional and thus data and resource hungry, we also intend to explore possible deep learning approaches which can capture the relevant variations in the EEG spectrum in a more parameter- and sample-efficient manner. Our first foray into this task are described in Stabile et al., 2025.

## 4.5 Conclusion

Our work provides evidence of the ability to predict fMRI motor brain activity from EEG recordings alone across different days, in both task-evoked and spontaneous conditions, with statistical significance in individual subjects. These results present an important contribution to the literature, with potential for translation to EEG neurofeedback applications.

## 5 Acknowledgments

Funding by grants LARSyS (FCT, DOI: 10.54499/LA/P/0083/2020, 10.54499/UIDP/50009/2020), MIGN2Treat (FCT, PTDC/EMD-EMD/29675/2017 and LISBOA-01-0145-FEDER-029675), NeurAugVR (FCT, PTDC/CCI-COM/31485/2017), PRR Center for Responsible AI (C645008882-00000055), and FCT grant SFRH/BD/151128/2021.

## References

Abreu, R., Jorge, J., Leal, A., Koenig, T., & Figueiredo, P. (2021). Eeg microstates predict concurrent fmri dynamic functional connectivity states. *Brain Topography*, 34(1), 41–55. <https://doi.org/10.1007/s10548-020-00805-1>

Abreu, R., Leal, A., & Figueiredo, P. (2018). Eeg-informed fmri: A review of data analysis methods. *Frontiers in Human Neuroscience*, 12. <https://doi.org/10.3389/fnhum.2018.00029>

Abreu, R., Leite, M., Jorge, J., Grouiller, F., van der Zwaag, W., Leal, A., & Figueiredo, P. (2016). Ballistocardiogram artifact correction taking into account physiological signal preservation in simultaneous eeg-fmri. *Neuroimage*, 135, 45–63. <https://www.sciencedirect.com/science/article/pii/S1053811916002391>

Afrasiyabi, A., Bhaskar, D., Busch, E. L., Caplette, L., Singh, R., Lajoie, G., Turk-Browne, N. B., & Krishnaswamy, S. (2025). Latent representation learning for multimodal brain activity translation. *ICASSP 2025 - 2025 IEEE International Conference on Acoustics, Speech and Signal Processing (ICASSP)*, 1–5. <https://doi.org/10.1109/ICASSP49660.2025.10887834>

Batista, D., Caetano, G., Fleury, M., Figueiredo, P., & and, A. V. (2024). Effect of head-mounted virtual reality and vibrotactile feedback in erd during motor imagery brain–computer interface training. *Brain-Computer Interfaces*, 11(1-2), 11–20. <https://doi.org/10.1080/2326263X.2023.2264000>

Bertrand, O., & Tallon-Baudry, C. (2000). Oscillatory gamma activity in humans: A possible role for object representation. *International Journal of Psychophysiology*, 38(3), 211–223. <https://www.sciencedirect.com/science/article/pii/S0167876000001665>

Caetano, G., Esteves, I., Vourvopoulos, A., Fleury, M., & Figueiredo, P. (2023). Neuxus open-source tool for real-time artifact reduction in simultaneous eeg-fmri. *NeuroImage*, 280, 120353. <https://doi.org/https://doi.org/10.1016/j.neuroimage.2023.120353>

Calhas, D., & Henriques, R. (2020). Eeg to fmri synthesis: Is deep learning a candidate? <https://arxiv.org/abs/2009.14133>

Calhas, D., & Henriques, R. (2022a). Eeg to fmri synthesis benefits from attentional graphs of electrode relationships. <https://arxiv.org/abs/2203.03481>

Calhas, D., & Henriques, R. (2022b). Eeg to fmri synthesis benefits from attentional graphs of electrode relationships. <https://arxiv.org/abs/2203.03481>

Calhas, D., & Henriques, R. (2023). Eeg to fmri synthesis for medical decision support: A case study on schizophrenia diagnosis. *medRxiv*. <https://doi.org/10.1101/2023.08.07.23293748>

Chang, C.-Y., Hsu, S.-H., Pion-Tonachini, L., & Jung, T.-P. (2020). Evaluation of artifact subspace reconstruction for automatic artifact components removal in multi-channel eeg recordings. *IEEE Transactions on Biomedical Engineering*, 67(4), 1114–1121. <https://doi.org/10.1109/TBME.2019.2930186>

Cury, C., PierreMaurel, Gribonval, R., & Barillot, C. (2020). A sparse eeg-informed fmri model for hybrid eeg-fmri neurofeedback prediction. *Frontiers in Neuroscience*, 13. <https://www.frontiersin.org/journals/neuroscience/articles/10.3389/fnins.2019.01451>

Deligianni, F., Centeno, M., Carmichael, D. W., & D. Clayden, J. (2014). Relating resting-state fmri and eeg whole-brain connectomes across frequency bands. *Frontiers in Neuroscience*, 8. <https://doi.org/10.3389/fnins.2014.00258>

Delorme, A., & Makeig, S. (2004). Eeglab: An open source toolbox for analysis of single-trial eeg dynamics including independent component analysis. *Journal of Neuroscience Methods*, 134(1), 9–21. <https://www.sciencedirect.com/science/article/pii/S0165027003003479>

Fleury, M., Figueiredo, P., Vourvopoulos, A., & Lécuyer, A. (2023). Two is better? combining eeg and fmri for bci and neurofeedback: A systematic review. *Journal of Neural Engineering*, 20(5), 051003. <https://doi.org/10.1088/1741-2552/ad06e1>

Formaggio, E., Storti, S. F., Cerini, R., Fiaschi, A., & Manganotti, P. (2010). Brain oscillatory activity during motor imagery in eeg-fmri coregistration. *Magnetic Resonance Imaging*, 28(10), 1403–1412. [https://doi.org/https://doi.org/10.1016/j.mri.2010.06.030](https://doi.org/10.1016/j.mri.2010.06.030)

Jenkinson, M., Bannister, P., Brady, M., & Smith, S. (2002). Improved optimization for the robust and accurate linear registration and motion correction of brain images. *NeuroImage*, 17(2), 825–841. <https://www.sciencedirect.com/science/article/pii/S1053811902911328>

Jorge, J., van der Zwaag, W., & Figueiredo, P. (2014). Eeg–fmri integration for the study of human brain function [Multimodal Data Fusion]. *NeuroImage*, 102, 24–34. [https://doi.org/https://doi.org/10.1016/j.neuroimage.2013.05.114](https://doi.org/10.1016/j.neuroimage.2013.05.114)

Keynan, J. N., Meir-Hasson, Y., Gilam, G., Cohen, A., Jackont, G., Kinreich, S., Ikar, L., Or-Borichev, A., Etkin, A., Gyurak, A., Klovatch, I., Intrator, N., & Hendl, T. (2016). Limbic activity modulation guided by functional magnetic resonance imaging–inspired electroencephalography improves implicit emotion regulation [New Insight Into Depression Therapeutics]. *Biological Psychiatry*, 80(6), 490–496. <https://doi.org/https://doi.org/10.1016/j.biopsych.2015.12.024>

Kovalev, A., Mikheev, I., & Ossadtchi, A. (2022). Fmri from eeg is only deep learning away: The use of interpretable dl to unravel eeg-fmri relationships. <https://arxiv.org/abs/2211.02024>

Lancaster, G., Iatsenko, D., Pidde, A., Ticcinelli, V., & Stefanovska, A. (2018). Surrogate data for hypothesis testing of physical systems [Surrogate data for hypothesis testing of physical systems]. *Physics Reports*, 748, 1–60. <https://www.sciencedirect.com/science/article/pii/S0370157318301340>

Legeay, S., Caetano, G., Figueiredo, P., & Vourvopoulos, A. (2022). Neuxus: A biosignal processing and classification pipeline for real-time brain-computer interaction. *2022 IEEE 21st Mediterranean Electrotechnical Conference (MELECON)*, 424–429. <https://doi.org/10.1109/MELECON53508.2022.9842925>

Li, Y., Lou, A., Xu, Z., Wang, S., & Chang, C. (2024). Leveraging sinusoidal representation networks to predict fmri signals from eeg. <https://arxiv.org/abs/2311.04234>

Li, Y., Lou, A., Xu, Z., Zhang, S., Wang, S., Englot, D. J., Kolouri, S., Moyer, D., Bayrak, R. G., & Chang, C. (2024). Neurobolt: Resting-state eeg-to-fmri synthesis with multi-dimensional feature mapping. In A. Globerson, L. Mackey, D. Belgrave, A. Fan, U. Paquet, J. Tomczak, & C. Zhang (Eds.), *Advances in neural information processing systems* (pp. 23378–23405, Vol. 37). Curran Associates, Inc. [https://proceedings.neurips.cc/paper\\_files/paper/2024/file/29c294ddc628c94cd2c636383ef106c1-Paper-Conference.pdf](https://proceedings.neurips.cc/paper_files/paper/2024/file/29c294ddc628c94cd2c636383ef106c1-Paper-Conference.pdf)

Liu, X., Hong, L., & Sajda, P. (2020). Latent neural source recovery via transcoding of simultaneous eeg-fmri. <https://arxiv.org/abs/2010.02167>

Liu, X., Tu, T., & Sajda, P. (2022). Inferring latent neural sources via deep transcoding of simultaneously acquired eeg and fmri. <https://arxiv.org/abs/2212.02226>

Logothetis, N. K., Pauls, J., Augath, M., Trinath, T., & Oeltermann, A. (2001). Neurophysiological investigation of the basis of the fmri signal. *Nature*, 412, 150–157. <https://api.semanticscholar.org/CorpusID:969175>

MathWorks. (2023). *Matlab (r2023b)*. Natick, Massachusetts, United States. <https://www.mathworks.com>

Meir-Hasson, Y., Keynan, J. N., Kinreich, S., Jackont, G., Cohen, A., Ilana Podlipsky-Klovatch, T. H., & Intrator, N. (2016). One-class fmri-inspired eeg model for self-regulation training. *PLoS One*, 11. <https://doi.org/10.1371/journal.pone.0154968>

Meir-Hasson, Y., Kinreich, S., Podlipsky, I., Hendl, T., & Intrator, N. (2014). An eeg finger-print of fmri deep regional activation [Multimodal Data Fusion]. *NeuroImage*, 102, 128–141. <https://www.sciencedirect.com/science/article/pii/S1053811913010963>

Moe, Y. (2019). *Efficient group lasso in python*. <https://github.com/yngvem/group-lasso>

Murta, T., Leite, M., Carmichael, D., Figueiredo, P., & Lemieux, L. (2015). Electrophysiological correlates of the bold signal for eeg-informed fmri [© 2014 The Authors Human Brain Mapping Published by Wiley Periodicals, Inc.]. *Human Brain Mapping*, 36(1), 391–414. <https://doi.org/10.1002/hbm.22623>

Nogueira, F. (2014). Bayesian optimization: Open source constrained global optimization tool for python. <https://github.com/bayesian-optimization/BayesianOptimization>

Nunes, J. D., Vourvopoulos, A., Blanco-Mora, D. A., Jorge, C., Fernandes, J.-C., i Badia, S. B., & Figueiredo, P. (2023). Brain activation by a vr-based motor imagery and observation task: An fmri study. *PLoS ONE*, 18(9), 1–18. <https://doi.org/10.1371/journal.pone.0291528>

Olszowy, W., Aston, J., Rua, C., & Williams, G. B. (2019). Accurate autocorrelation modeling substantially improves fmri reliability. *Nature Communications*, 10. <https://doi.org/10.1038/s41467-019-09230-w>

Or-Borichev, A., Gurevitch, G., Klovatch, I., Greental, A., Lerner, Y., Levy, D. J., & Hendl, T. (2023). Neural and functional validation of fmri-informed eeg model of right inferior frontal gyrus activity. *NeuroImage*, 266, 119822. <https://doi.org/https://doi.org/10.1016/j.neuroimage.2022.119822>

Pantazis, D., Nichols, T. E., Baillet, S., & Leahy, R. M. (2005). A comparison of random field theory and permutation methods for the statistical analysis of meg data. *NeuroImage*, 25(2), 383–394. <https://www.sciencedirect.com/science/article/pii/S1053811904005671>

Pfurtscheller, G., & Lopes da Silva, F. (1999). Event-related eeg/meg synchronization and desynchronization: Basic principles. *Clinical Neurophysiology*, 110(11), 1842–1857. [https://doi.org/https://doi.org/10.1016/S1388-2457\(99\)00141-8](https://doi.org/https://doi.org/10.1016/S1388-2457(99)00141-8)

Pfurtscheller, G., Brunner, C., Schlogl, A., & Lopes da Silva, F. (2006). Mu rhythm (de)synchronization and eeg single-trial classification of different motor imagery tasks. *NeuroImage*, 31(1), 153–159. <https://doi.org/https://doi.org/10.1016/j.neuroimage.2005.12.003>

Roos, K. G., Fukuda, A., & Cap, Q. H. (2025). From brainwaves to brain scans: A robust neural network for eeg-to-fmri synthesis. <https://arxiv.org/abs/2502.08025>

Rudnev, V., Melnikov, M., Savelov, A., Shtark, M., & Sokhadze, E. (2021). Fmri-eeg fingerprint regression model for motor cortex. *NeuroRegulation*, 8, 3. <https://doi.org/https://doi.org/10.15540/nr.8.3.162>

Scheeringa, R., Petersson, K., Kleinschmidt, A., Jensen, O., & Bastiaansen, M. (2012). Eeg alpha power modulation of fmri resting state connectivity. *Brain Connectivity*, 2(5), 254–264. <https://doi.org/10.1089/brain.2012.0088>

Simões, M., Abreu, R., Direito, B., Sayal, A., Castelhano, J., Carvalho, P., & Castelo-Branco, M. (2020). How much of the bold-fmri signal can be approximated from simultaneous eeg data: Relevance for the transfer and dissemination of neurofeedback interventions. *Journal of Neural Engineering*, 17(4), 046007. <https://dx.doi.org/10.1088/1741-2552/ab9a98>

Simon, N., Friedman, J., Hastie, T., & Tibshirani, R. (2013). A sparse-group lasso. *Journal of Computational and Graphical Statistics*, 22(2), 231–245. <https://doi.org/10.1080/10618600.2012.681250>

Singer, N., Poker, G., Dunsky-Moran, N., Nemni, S., Reznik Balter, S., Doron, M., Baker, T., Dagher, A., Zatorre, R. J., & Hendler, T. (2023). Development and validation of an fmri-informed eeg model of reward-related ventral striatum activation. *NeuroImage*, 276, 120183. <https://doi.org/https://doi.org/10.1016/j.neuroimage.2023.120183>

Smith, S. M., Jenkinson, M., Woolrich, M. W., Beckmann, C. F., Behrens, T. E., Johansen-Berg, H., Bannister, P. R., De Luca, M., Drobniak, I., Flitney, D. E., Niazy, R. K., Saunders, J., Vickers, J., Zhang, Y., De Stefano, N., Brady, J. M., & Matthews, P. M. (2004). Advances in functional and structural mr image analysis and implementation as fsl. *NeuroImage*, 23, S208–S219. <https://www.sciencedirect.com/science/article/pii/S1053811904003933>

Stabile, P., Mehta, N., Gonçalves, I., Farabbi, A., Vourvopoulos, A., Grover, P., & Figueiredo, P. (2025). Deep learning prediction of bold-fmri signals from simultaneous eeg during motor imagery. *EU-SIPCO*. <https://www.politesi.polimi.it/handle/10589/223505>

Tadel, F., Baillet, S., Mosher, J. C., Pantazis, D., & Leahy, R. M. (2011). Brainstorm: A user-friendly application for meg/eeg analysis. *Intell. Neuroscience*, 2011. <https://doi.org/10.1155/2011/879716>

Vourvopoulos, A., Ferreira, A., & i Badia, S. B. Neurow: An immersive vr environment for motor-imagery training with the use of brain-computer interfaces and vibrotactile feedback. In: In *Proceedings of the 3rd international conference on physiological computing systems - volume 1: Phycs*. INSTICC. SciTePress, 2016, 43–53. ISBN: 978-989-758-197-7. <https://doi.org/10.5220/0005939400430053>

Vourvopoulos, A., Jorge, C., Abreu, R., Figueiredo, P., Fernandes, J.-C., & i Badia, S. B. (2019). Efficacy and brain imaging correlates of an immersive motor imagery bci-driven vr system for upper limb motor rehabilitation: A clinical case report. *Frontiers in Human Neuroscience, Volume 13*. <https://doi.org/10.3389/fnhum.2019.00244>

Wang, Y., & Li, T.-Q. (2015). Dimensionality of ica in resting-state fmri investigated by feature optimized classification of independent components with svm. *Frontiers in Human Neuroscience*, 9. <https://www.frontiersin.org/articles/10.3389/fnhum.2015.00259>

Warbrick, T. (2022). Simultaneous eeg-fmri: What have we learned and what does the future hold? *Sensors (Basel)*, 22, 2262. <https://doi.org/10.3390/s22062262>

Yao, W., Lyu, Z., Mahmud, M., Zhong, N., Lei, B., & Wang, S. (2025). Catd: Unified representation learning for eeg-to-fmri cross-modal generation. *IEEE Transactions on Medical Imaging*, 1–1. <https://doi.org/10.1109/TMI.2025.3550206>

Yeo, B. T. T., Krienen, F. M., Sepulcre, J., Sabuncu, M. R., Lashkari, D., Hollinshead, M., Roffman, J. L., Smoller, J. W., Zöllei, L., Polimeni, J. R., Fischl, B., Liu, H., & Buckner, R. L. (2011). The organization of the human cerebral cortex estimated by intrinsic functional connectivity. *Journal of Neurophysiology*, 106(3), 1125–1165. <https://doi.org/10.1152/jn.00338.2011>

Zoubi, O. A., Mayeli, A., Misaki, M., Tsuchiyagaito, A., Zotev, V., 1000, I. T., Refai, H., Paulus, M., & Bodurka, J. (2022). Canonical eeg microstates transitions reflect switching among bold resting state networks and predict fmri signal. *Journal of Neural Engineering*, 18(6), 066051. <https://doi.org/10.1088/1741-2552/ac4595>